JOURNAL OF AIRCRAFT
Vol. 59, No. 6, November–December 2022

Aeromechanical Analysis of a Next-Generation Mars Hexacopter Rotor

Cheng Chi,* Ravi Lumba,† Yong Su Jung,‡ and Anubhav Datta§
University of Maryland, College Park, Maryland 20740

https://doi.org/10.2514/1.C036739

A three-dimensional (3D) aeromechanical analysis is carried out on the rotor blades of a 20 kg conceptual Mars Hexacopter. The objectives are to understand the aeroelastic behavior of its unique ultrathin low-Reynolds-number and high-Mach-number blades and study the interactions of structures, aerodynamics, and control moments in the Martian atmosphere. Beginning with structural analysis in vacuum, comprehensive analysis is carried out in hover and forward flight using 3D Finite Element Method (FEM), three-dimensional (2D) airfoil tables, and free wake. Natural frequencies of the rotor, elastic response of the blade, control moments at the root, airloads of blade sections, and 3D stresses are studied. Two types of designs are considered: a baseline design with pitch axis at the quarter chord and an unconventional design with the pitch axis moved to the midchord. Unusual nose-up elastic twist is observed on the rotor blades that appears to stem from the trapeze effect that counteracts the flattening effect of the propeller moment. By moving the pitch axis to midchord, the control moment is reduced by 30–40% without any noticeable adverse effect on stability due to the low Lock number. Both designs have maximum stresses well below the material limits, but the midchord design has a more uniform distribution of stress in general and lower levels of shear stress in particular. These and many other unconventional phenomena make Martian aeromechanics unique and ripe with possibilities of innovations tailored to its atmosphere.

Nomenclature

C_c	=	chordwise aerodynamic force coefficient
C_m	=	moment aerodynamic coefficient
C_n	=	normal aerodynamic force coefficient
C_P	=	power coefficient
C_T	=	thrust coefficient
c	=	blade chord, m
e	=	equivalent flap hinge offset, m
I_β	=	second moment of inertia of flapping, $\mathrm{kg \cdot m^2}$
K_β	=	equivalent flap hinge stiffness, $(\mathrm{N \cdot m})/\mathrm{rad}$
M_{tip}	=	blade tip Mach number
R	=	rotor radius, m
Re	=	Reynolds number
S_β	=	first moment of inertia of flapping, $\mathrm{kg \cdot m}$
t	=	blade thickness, m
α	=	angle of attack, deg
α_s	=	shaft tilt angle, deg
γ	=	Lock number
γ_{xy}	=	shear stress, $\mathrm{N/m^2}$
ζ	=	damping ratio
θ_{75}	=	collective pitch at 75% radius, deg
μ	=	advance ratio
ν_β	=	flap frequency
σ	=	rotor solidity
σ_{xx}	=	axial stress, $\mathrm{N/m^2}$
ψ	=	azimuth angle, deg

I. Introduction

THE first successful flight of the JPL/NASA/AeroVironment Mars Helicopter (MH) Ingenuity on 19 April 2021 opened a new chapter in Mars exploration. The dream of rotorcraft flight on Mars [1–7] has been realized, and the future of Mars exploration revolutionized.

The 1.8 kg MH is a technology demonstrator with no payload, designed to inform our understanding of basic Martian aeronautics [8,9]. Science missions will require larger platforms with longer endurance and greater payload. NASA Ames Research Center and Jet Propulsion Laboratory have proposed conceptual designs as follow-ons to MH with the University of Maryland carrying out preliminary structural design of the rotor blades [10]. Two configurations were proposed: a coaxial and a hexacopter. They cover seven designs as presented in Table 1. The MH is listed for comparison. Two designs use coaxial rotors: a 4.6 kg Advanced Mars Helicopter (AMH) with the same rotor radius as MH and a 19.3 kg Mars Science Helicopter (MSH) with a rotor radius of 1.25 m. The other five designs are the hexacopters with a rotor radius of 0.64 m, each optimized for a different payload, range, and landing site.

The preliminary structural design of the MSH Coaxial and the MSH Hexacopter baseline rotors, along with aerodynamic analysis of their unique airfoils, was reported in Ref. [11]. The requirement to produce a target flap frequency is based on the bandwidth criterion on the current Mars Helicopter: 275 rad/s [12]. Only thrust control (collective pitch or rpm control) is required for the hexacopter rotors. It turns out then only the coning mode frequency of the hexacopter rotor must be greater than 275 rad/s, which for the design rotor speed of 2782 rpm is 1.06/rev. Both collective and cyclic control is needed for the coaxial rotor. It turns out then the regressive flap mode frequency must be greater than 275 rad/s, which for the design rotor speed of 1425 rpm is as high as 2.8/rev. It was observed that the lower frequency of the hexacopter generally produced lower blade weight [11]. The blade frequency requirement and the weight budget could only be met by the hexacopter. Therefore, the focus of this paper is on the hexacopter. The configuration, taken from Ref. [10], is reproduced in Fig. 1.

The understanding of the three-dimensional (3D) aeroelastic behavior of ultralight, ultrathin, sharp-edged rotors is essential to design larger aircraft on Mars. The rotor aerodynamic design and

Received 6 November 2021; revision received 24 March 2022; accepted for publication 14 April 2022; published online 12 May 2022.

*Alfred Gessow Rotorcraft Center; currently Graduate Research Assistant, Aerospace Engineering, University of Maryland, 3179 Glenn L. Martin Hall, College Park, Maryland 20742.

†Alfred Gessow Rotorcraft Center; currently National Science Foundation Fellow, Aerospace Engineering, University of Maryland, 3179 Glenn L. Martin Hall, College Park, Maryland 20742.

‡Alfred Gessow Rotorcraft Center; currently Post-Doctoral Associate, Aerospace Engineering, University of Maryland, 3179 Glenn L. Martin Hall, College Park, Maryland 20742.

§Alfred Gessow Rotorcraft Center; currently Associate Professor, Aerospace Engineering, University of Maryland, 3179 Glenn L. Martin Hall, College Park, Maryland 20742.

Table 1 Family of next-generation Mars helicopter designs by NASA [10]

Aircraft	Radius, m	Mass, kg	Payload, kg
MH	0.605	1.8	0
AMH	0.605	4.6	1.3
MSH Coax	1.25	19.3	2.02
MSH Hexa Baseline	0.64	17.7	2.02
MSH Hexa Max cap[a]	0.64	31.2	0, 2, 5, 8
MSH Hexa Milankovic[b]	0.64	17.12	2.1
MSH Hexa Becquerel[b]	0.64	20.73	2.7
MSH Hexa Palikir[b]	0.64	21.03	2.1

[a]Maximum capacity of various ranges.
[b]Names of crater on Mars.

Fig. 1 Hexacopter MSH configurations by NASA [10].

airfoils were designed by NASA Ames specifically for Mars [10,13]. The structural design and aeromechanical analysis presented in this paper extracts low-Reynolds-number/high-Mach-number decks of these airfoils to use with free wake and a full 3D description of the structure. Performance, airloads, response, stability, and 3D dynamic stresses are predicted. Particular emphasis is placed on the placement of the pitch axis to take advantage of the Mars atmosphere to relieve blade stresses and reduce weight. The blade design is unique and unusual, with few test data for guidance, so systematic step-by-step analysis is needed. The purpose of this paper is to document the key findings of the work reported in Refs. [11,14]

II. Technical Approach

The structural design of the blade and hub is discussed before the detailed analysis begins. In addition to the baseline design (pitch axis at quarter chord), an alternative design with the pitch axis at midchord was developed to reduce the root loads. Next, a detailed 3D finite element analysis (FEA) is carried out to investigate the natural frequencies, root loads, and blade deformation due to rotation in vacuum. This is followed by aeromechanical analysis using 3D FEA in hover and forward flight. Performance, airloads, control load, and 3D stresses of both blade designs are compared and discussed. The airfoil decks needed in the analysis were obtained from 2D CFD. Only an isolated rotor was considered in this study, though Ref. [10] details coaxial helicopter and hexacopter configurations. This focus on an isolated rotor is deemed acceptable for initial rotor blade structural and dynamic analysis. Rotor-to-rotor multirotor aerodynamic interactions, though non-negligible, are considered to have a secondary influence on this overall analysis. The thrust in forward flight was obtained from a lower-order multirotor free-flight trim model. Throughout this study particular attention is paid on the effect of moving the pitch axis from quarter chord (conventional) to midchord (unusual).

III. Analysis Tools

The CAD designs were constructed in CATIA, with the same materials and knock-down factors used as the MH rotor blade [8,9,15]. Assessment of manufacturability is based on Maryland's long history of fabricating and wind-tunnel testing Mach-scale helicopter and tiltrotor blades. The flexible parts of the design were meshed in Cubit with higher-order hexahedral elements and the pitch bearing modeled as a multibody joint. The analysis used the U.S. Army/University of Maryland code X3D [16,17]. X3D has a built-in lifting-line/free-wake aerodynamics model interface with the 3D structure. To verify the interface under Martian conditions, hover performance was predicted and compared with test data from a rotor fabricated and tested in a small vacuum chamber in-house [15]. This small-scale rotor had a 2% thickness ratio and a 6% cambered arc airfoil. The figure of merit and coefficient of power were compared against the experimental data, showing reasonable agreement (Fig. 2).

For the hexacopter blade, a set of consistent low-Reynolds-number/high-Mach-number airfoil decks were prepared using the University of Maryland unstructured Reynolds-averaged Navier–Stokes (RANS) solver HAMSTR [18]. This part of the work complements earlier airfoil work performed/documented in Ref. [13]. The HAMSTR solver was validated against Mars airfoils with experimental data from Ref. [19] and reported in our previous study [11]. The blade was divided up into five regions, each with its own unique airfoil, Mach number M, and Reynolds number Re. Airfoil decks for each region were generated and documented [14]. For each deck, the aerodynamic coefficients are functions of angle of attack and Mach number with a fixed Re/M ratio. Within each region, fine-tuning to the local Reynolds number was based on standard correction [20].

In forward flight, the rotor is trimmed to a particular thrust. For a hexacopter, each rotor will have its own thrust in a steady level flight. To find an estimate of this thrust, an in-house multirotor free-flight trim model was used with rigid flapping (first flap frequency from

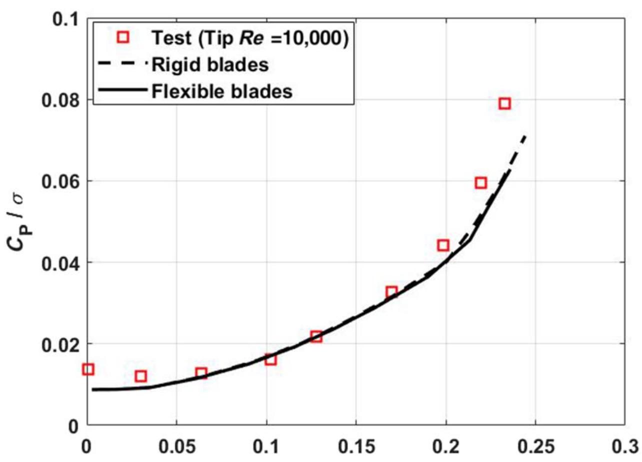

a) Power coefficient

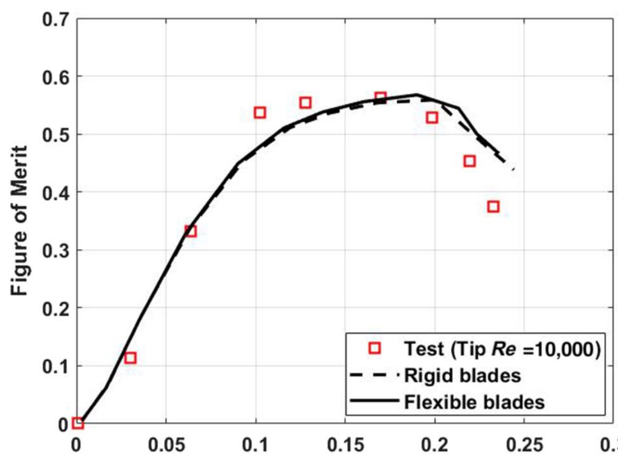

b) Figure of merit

Fig. 2 Comparison of X3D prediction and experimental results for Mars model rotor [15].

X3D), 2D airfoil decks, and uniform inflow with no rotor-to-rotor interactions. The analysis predicted the trimmed aircraft attitudes and rotor thrust. These were used later to trim an isolated rotor in X3D. Thus, analysis carrying all six rotors with 3D models was avoided. The assumption of no interactions is a poor one and should be re-examined in the future. At present it was deemed adequate.

IV. Hub Mechanical and Blade Structural Design

The hexacopter has six four-bladed hingeless rotors with a radius of $R = 0.64$ m, a solidity of $\sigma = 0.142$, and a tip Mach number of $M_{\mathrm{tip}} = 0.8$. The rotor parameters are summarized in Table 2. For a multicopter (four or more rotors), the vehicle can be controlled only by the thrust produced by the rotors. Therefore, only collective or rotor speed control is needed. The tip Mach number is carefully selected by NASA to optimized rotor performance, and the need to avoid frequency crossings mean revolution per minute (RPM) control is a nonstarter. Moreover, the tip Mach number of the rotor design is 0.8 in hover, limiting the RPM margin. Therefore, the hexacopter uses collective pitch. A conceptual rotor hub with pitch control is shown in Fig. 3a.

The connection between the blade root and the rotor hub is illustrated in Fig. 3b. The root of each blade is surrounded by a pitch bearing, which is secured by a hub tube. The thread of a two-in-one thrust-bearing screw goes through the yoke rigid end into the blade root insert screw hole. Each center yoke connects two blades via the thrust bearing. A pitch horn is located outside of the hub tube and fixed to the blade root. The blade flap and lag bending moments and shear forces are transferred through the pitch bearing into the hub tube. The blade centrifugal force is carried by the thrust bearing screw, which is eventually secured by the center yokes in the hub. The blade torsion moment is transferred via the pitch horn to the pitch link. The hub tube and center yoke are secured to the hub.

Two blade designs were developed and analyzed. The first one is a baseline design with the pitch axis (P.A.) located at quarter chord. The resultant large chordwise center of gravity (C.G.) offset stem from the limited internal space (leading-edge weight not feasible) generates a high control load from propeller moment and potentially increases the weight of the hub and control system. Therefore, a second design —with the pitch axis relocated to midchord—is considered. The geometry for both blade designs is shown in Fig. 4.

The chord (solid line) and the built-in twist (dashed line) distribution of the blade are shown in Fig. 5. The blade airfoils are shown in

Table 2 Rotor parameters

Parameter	Value
Number of blades	4
Radius	0.64 m
Solidity	0.142
Hub type	Hingeless
Tip Mach	0.8
Flap frequency	1.2/rev

Fig. 4 Blade meshes of two blade designs.

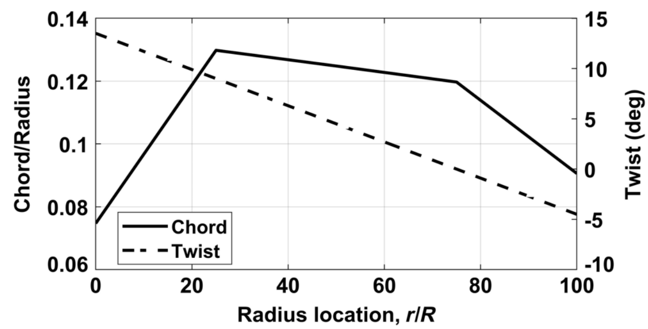

Fig. 5 Chord and twist distribution designed by NASA [10].

Fig. 6. These blade design parameters and unconventional airfoils were designed by NASA to optimize the rotor performance in the Martian atmosphere. Two 8% thickness-to-chord diamond airfoils are used at 9% R and 25% R. Two 1% thickness-to-chord cambered airfoils are used at 50% R and 75–100% R. The selection of sharp-edged, thin-plate, cambered, and triangular profiles over Earth-like airfoils are based on a greater understanding of ultralow Re flows developed over the last decade [13,21,22].

Proper design of the internal structure and modification to sectional thickness were needed to meet the weight and frequency targets. The final blade structural design is demonstrated in Fig. 7. The weight estimation of this blade design is 50.4g, which is comparable to the weight estimation done by NASA Ames [10]. The skin consists of carbon fiber 60 gsm HR40 spread tow bidirectional $\pm 45°$ weave cloth with knocked-down modulus (measured modulus after fabrication reduced from manufacturer-provided value) from MH experience. It has seven layers of cloth at the root with a one ply drop-off up until 50% R. Outboard of 50% R, the skin has eight layers. Inside the skin, there is a spar made of MTM45-1 M46J 12K unidirectional tape. The spar ends at 45% R and has four layers of unidirectional tape at the root and a ply drop-off of two layers throughout the spar. Inside the spar, a foam core (Rohacell 31F foam) ends at 40% R. A cylindrical root insert (7075 aluminum) is secured by the skin and spar. The diameter, start, and end of the root is 2.5% R, 4% R, and 6% R, respectively. The meshes of both blade designs are shown in Fig. 8, and both of them consist of 1883 higher-order 27-noded hexahedral brick elements.

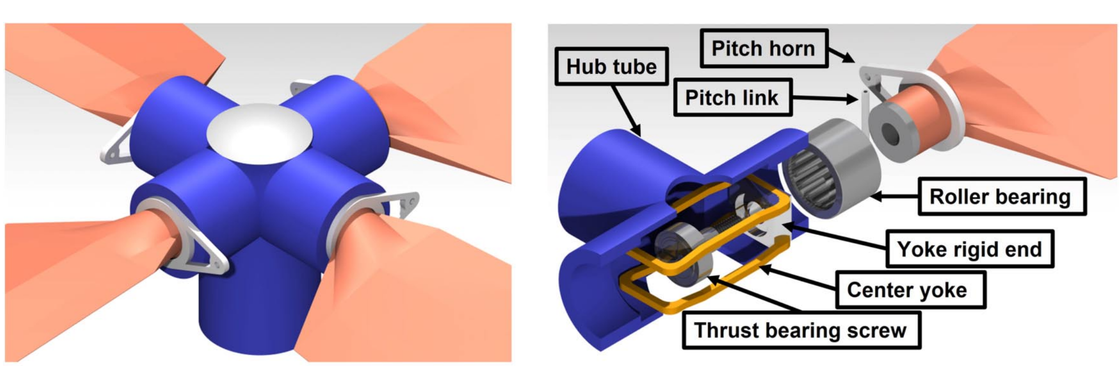

a) Rotor hub design **b) Blade root details**

Fig. 3 Rotor hub and blade root design.

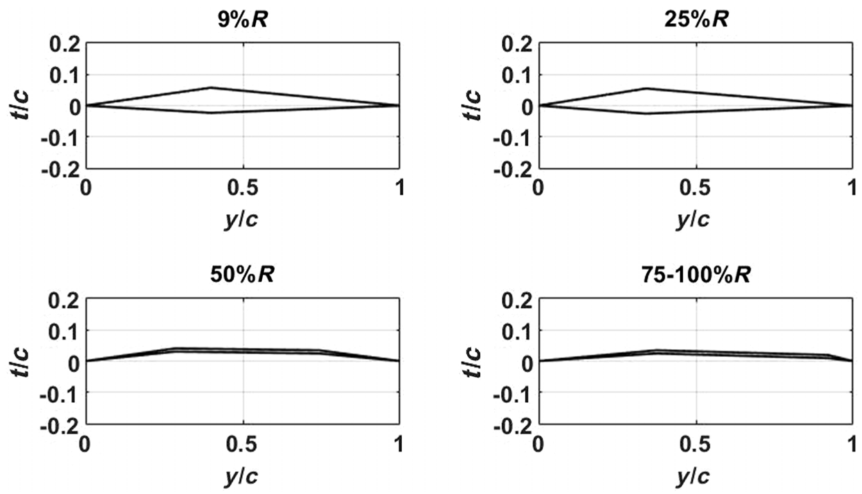

Fig. 6 Unconventional airfoils designed by NASA [13].

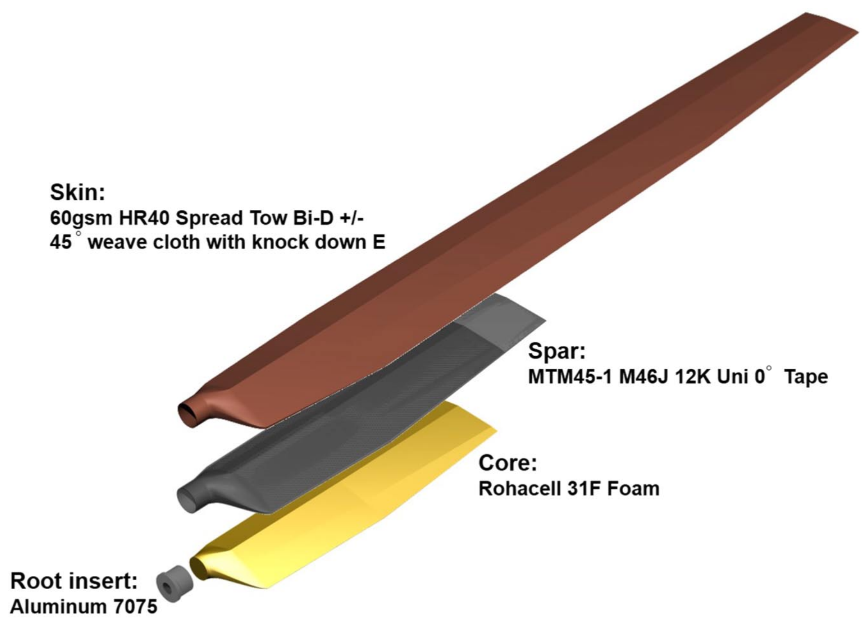

Fig. 7 Materials and internal structure of the blade design.

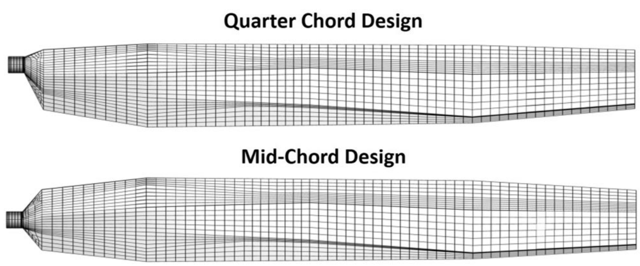

Fig. 8 Blade meshes of two blade designs.

Beam-like sectional properties, even though not required for the analysis in this paper, were important to understand the characteristic of the blade. Hence, the mass per length, chordwise C.G. location, normal mass moment of inertia per length, chordwise mass moment of inertia per length, sectional torsional stiffness, normal bending stiffness, and chordwise bending stiffness were extracted from the 3D structural model and documented in detail in Ref. [14]. However, because one of the areas of emphasis in this paper is the placement of the pitch axis, the chordwise C.G. location is included here (Fig. 9). The chordwise C.G. of the baseline design is located 20–30% c behind the pitch axis, whereas the C.G. offset of the midchord pitch axis design is much smaller.

V. Structural Analysis in Vacuum

This section examines the structural response in vacuum. Centrifugal force is the main load of a system with high rotational speed. Due to the low atmosphere density on Mars, higher rotor speed is needed to generate the required lift. Under this condition, the system is even more dominated by centrifugal force compared to the rotor systems on Earth. Hence, studying the behavior of blades in vacuum is important, as it allows for greater understanding of the inertial coupling caused due to unique blade design and pitch axis location without the complications of aerodynamics. Throughout the section, the effect of moving the pitch axis from $1/4$ chord to $1/2$ chord is emphasized.

A. Natural Frequencies

The fan plot for both blade designs is shown in Fig. 10. The first flap mode, denoted F1, which has a minimum requirement of 1.06/rev, easily meets this requirement and does not change between the two designs. The third flap mode, F3, also does not change near the operating RPM of 2800. Due to the change in C.G. offset, only the

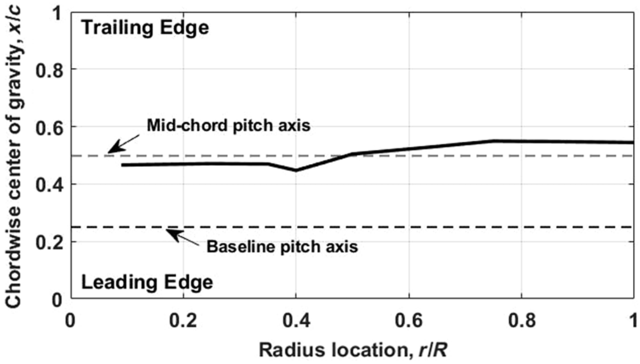

Fig. 9 Chordwise C.G. location.

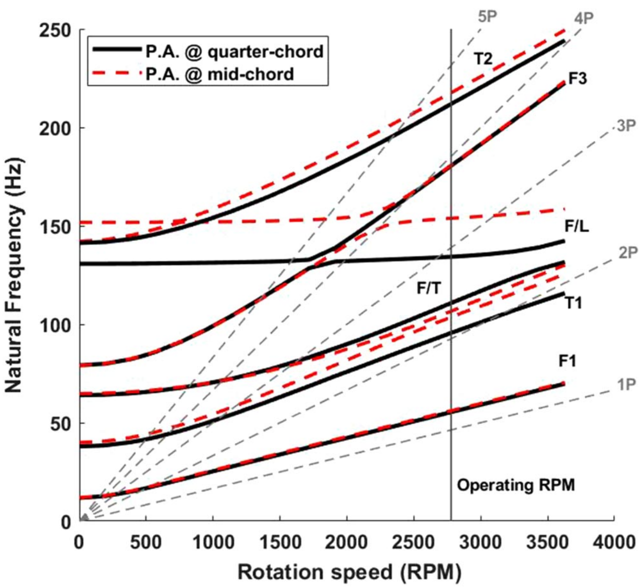

Fig. 10 Fan plot for both blade designs: F, flap; L, lag; T, torsion.

modes involving lag (L) and torsion (T) change when the pitch axis is moved from quarter chord to midchord. The first torsion (T1) mode increases from 2.06/rev to 2.23/rev at operating RPM, providing some stability benefits. The significant change is in the fourth mode, a coupled flag-lag (F/L) mode that increases from 2.89/rev to 3.31/rev.

B. Blade Root Loads

The steady blade root loads are presented in Table 3 for a case with a collective of 10°. The lead-lag force and blade pitching moment (highlighted) are the most affected by the relocation of the pitch axis. Because the C.G. remains close to midchord along the entire radius (Fig. 9), the in-plane component of the centrifugal force causes a large lag force. The lag force is independent of collective, as the change of C.G. with collective is negligible. By moving the pitch axis to midchord, the C.G. offset becomes very small, reducing the in-plane root shear by over an order of magnitude, which allows for a lighter hub design by relieving stresses. The reduction in torsional moment is due to the same mechanism: the elimination of the C.G. offset reduces the propeller moment on the blade.

Table 3 Blade root loads, $\theta_{75} = 10°$

		Pitch axis	
Root load	Sign convention	$1/4c$	$1/2c$
F_x (N)	+ve root to tip	874.5	874.5
F_y (N)	+ve leading edge	−64.27	4.5
F_z (N)	+ve up	0.0	0.0
$\boldsymbol{M_y}$ (N · m)	+ve nose up	−0.48	−0.32
M_y (N · m)	+ve flap down	−1.63	1.02
M_z (N · m)	+ve lead	-1×10^{-5}	1×10^{-5}

Figure 11 shows the variation of the blade control moment with collective for rotation in vacuum. In the collective range that would be expected for flight, the control moment is reduced by 30–40%. The reduction in control moment is important as it reduces the pitch link loads and allows for lighter servos. Previous designs required counterweights to alleviate the control moment, so moving the pitch axis will reduce the weight penalty of the counterweights.

C. Blade Deformation

Figure 12 shows the blade twist for a case with a collective of 5°. The blade has relatively little deflection until midspan, after which there is a large elastic twist. This is due to two reasons: the spar ending and the blade thickness reaching 1% t/c, which occur at 45%R and 50%R, respectively, and decrease the blade stiffness.

As shown in the previous section, the baseline design has a larger nose-down propeller moment, which explains why it has less nose-up elastic twist compared to the midchord model. However, both blades have a large elastic pitch-up twist, opposite to the expected response to the propeller moment. Due to the very low t/c of the blade, the trapeze effect was suspected to be the source, as it causes a pretwisted

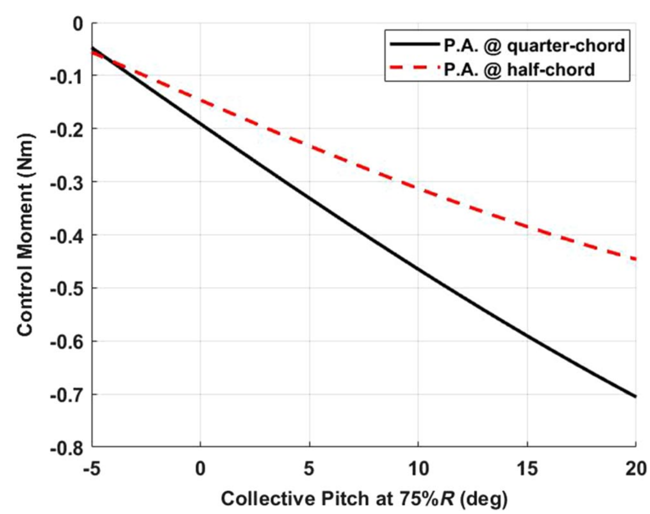

Fig. 11 Control moment vs collective.

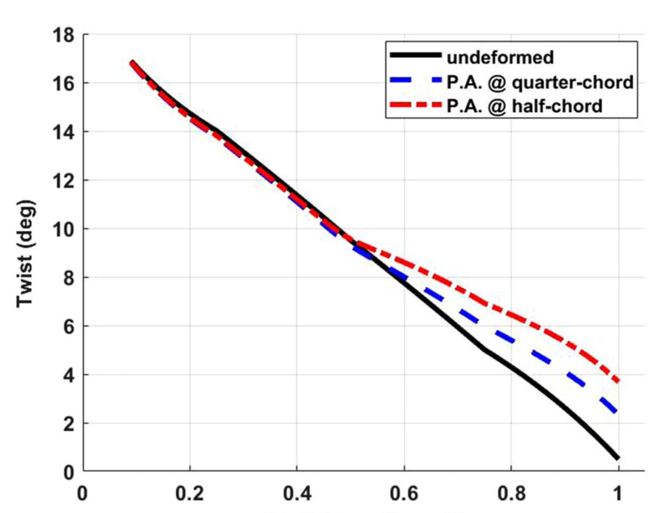

Fig. 12 Blade elastic twist for rotation in vacuum at $\theta_{75} = 5°$.

beam to untwist under a tensile load and is only prevalent for thin cross sections.

To investigate this effect, a simple aluminum blade model is created. The radius (0.64 m) and twist ($-18°$) are the same as the blade, with a similar aspect ratio of 10 being used. A uniform rectangular cross section with a thickness-to-chord ratio of 1% is used for the entire beam, which is equal to the blade outboard of $r/R = 0.5$. The pitch axis is placed at midchord.

For the trapeze effect, rotation is not required—a simple tensile force will suffice. A tensile tip force, equal to the centrifugal force at the beam root under a rotation speed of 120 rad/s, is applied. Figure 13 shows that the beam undergoes a large pitch-up elastic twist (untwisting). As expected, the deformation is independent of the collective, for the trapeze effect depends on the twist alone.

Under rotation, the trapeze effect and the propeller moment occur together. The trapeze effect will always try to untwist the blade and is dependent on the twist. The propeller moment will try to flatten the blade relative to the local chord line and is dependent on the local pitch angle (higher the pitch angle, higher the propeller moment). Figure 14 shows the twist deformation for the aluminum beam rotating in vacuum.

In Fig. 14, there are three different cases in how the propeller moment and trapeze effect combine. Case 1 is where the trapeze effect and propeller moment act together. This requires a negative collective to accompany the negative twist and is seen when $\theta_{75} = -40°$. The trapeze effect untwists the beam, and the propeller moment further attempts to flatten (in this case untwist) the beam. Case 2 involves the trapeze effect and propeller moment working against each other, with the propeller moment dominating. This occurs for large positive collectives, such as $\theta_{75} = 50°$, where the propeller moment is trying to flatten (further twist the blade) while the trapeze effect attempts to pitch up (untwist) the blade. Due to the large positive collective, the magnitude of the propeller moment is greater, and it overpowers the trapeze effect. Case 3 occurs for moderate pitch angles (such as $\theta_{75} = 5°$). This is where the MSH rotor is likely to operate. Here the propeller moment and trapeze effect work against each other, with the trapeze effect dominating. For these lower, but still positive, collectives the propeller moment is much smaller, while the trapeze effect is based on the twist, which has very limited change, resulting in a net pitch-up twist. This is the behavior noted in Fig. 12 and will be present in the expected collective range for this study.

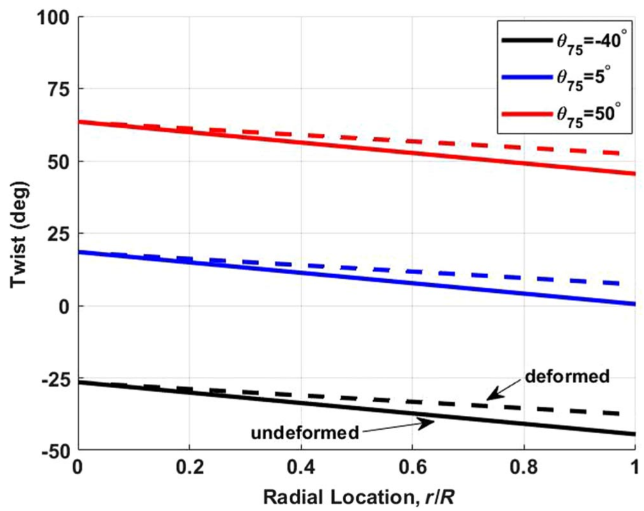

Fig. 13 Elastic twist response to extensional tip force for an aluminum beam.

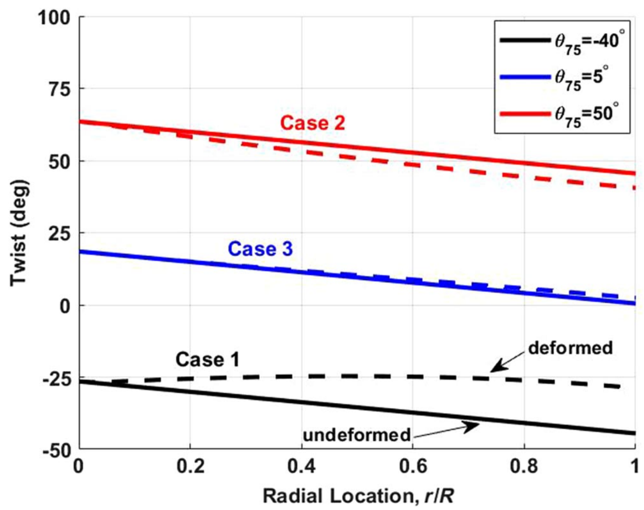

Fig. 14 Elastic twist for an aluminum beam rotating in vacuum.

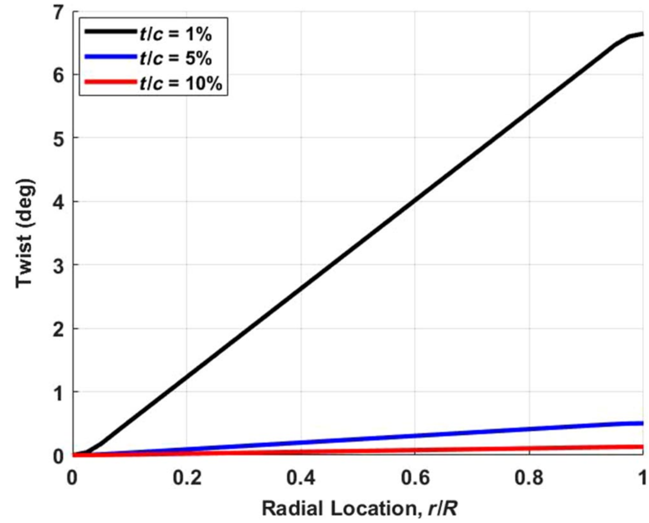

Fig. 15 Elastic twist due to axial extension (trapeze effect) for aluminum beams of varying thicknesses.

The elastic twist caused by the trapeze effect is insignificant for conventional rotors due to the larger torsional stiffness. Figure 15 shows the elastic twist for several aluminum beams with varying thickness-to-chord ratios. Note that the elastic twist is negligible for the thickest beam, as it is several orders of magnitude lower than for the one with a thin cross-section. However, this does indicate that in all future designs for Mars, or any other designs with thickness-to-chord ratios on the order of 1%, it might be beneficial to include the trapeze effect during analysis.

VI. Hover Analysis

Hover analysis is performed under the unique atmospheric conditions on Mars shown in Table 4, and over a range of collective pitch angles from 0 to 17° at an increment of 1°. Power and control moment are examined. Blade airloads, response, and 3D stresses are studied for a high thrust condition $C_T/\sigma = 0.12$.

A. Performance

Figure 16 shows the variation of blade loading with collective pitch. Without the structural model, there is obviously no difference in blade loading between the two designs. The flexible blades have higher blade loading than the rigid blades at the same collective due to pitch up introduced by the trapeze effect. The trends are similar

Table 4 Atmospheric conditions

Parameter	Mars (Jezero Crater)
Density (kg/m^3)	0.015
Speed of sound (m/s)	233.1
Dynamic viscosity ($N \cdot s/m^2$)	1.12×10^{-5}

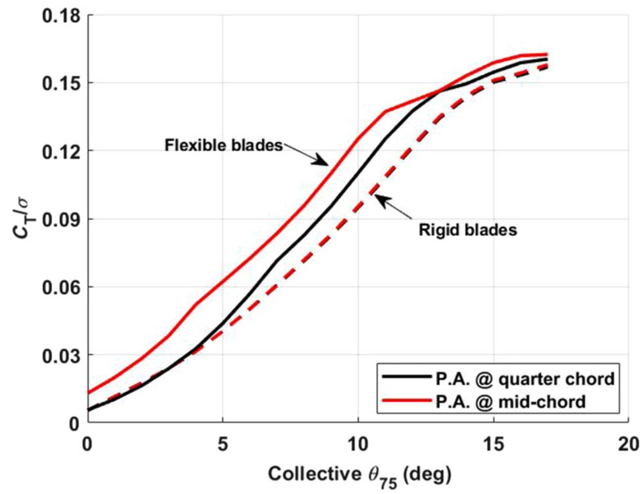

Fig. 16 Variation of blade loading with collective pitch.

among the two designs. However, the midchord design generates more thrust than the baseline design at the low to moderate collective pitch range.

Power coefficient (Fig. 17) and figure of merit (Fig. 18) are shown versus blade loading. As expected, there is again no difference between the two designs without introducing blade flexibility. The maximum figure of merit of the quarter chord design and the midchord design predicted by the flexible blade model is 0.645 and 0.636, respectively. The midchord design has a slightly earlier onset of stall.

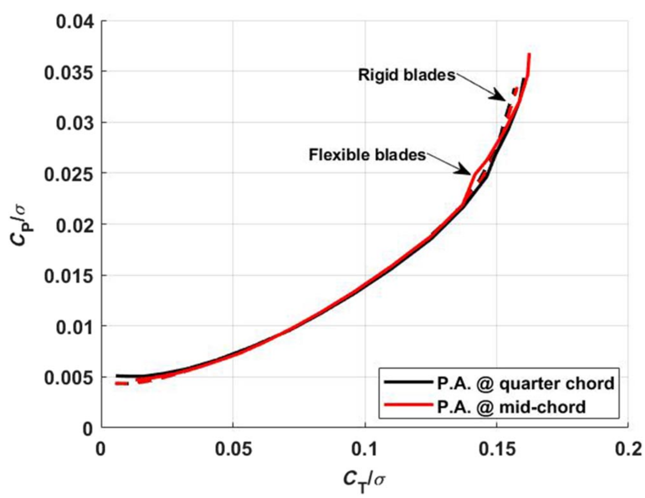

Fig. 17 Variation of power coefficient with blade loading.

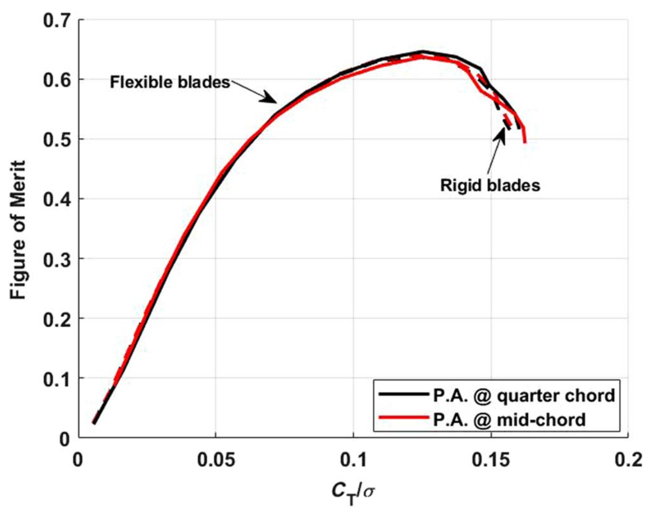

Fig. 18 Variation of figure of merit with blade loading.

B. Control Load

Figure 19 presents the variation in blade control moment with blade loading. The total control load in hover has the same trend as in pure rotation in vacuum. Considering a pitch horn length of 0.022 m (obtained from hub design in Fig. 3a), the pitch link of the baseline blade is under a constant compression load of 21.4 N, equivalent to 32.5% of the total lift needed to hover. However, a 30–40% reduction can be achieved by moving the pitch axis to midchord. The reduction in pitching moment is aided by the large aerodynamic center offset. With the aerodynamic center located ahead of the pitch axis, a nose-up aerodynamic pitching moment about the pitch axis is produced by the lift.

To further minimize the control load, blade root counterweights were sized for both pitch axis designs. A side view (from tip to root) of the quarter chord design blade is shown in Fig. 20. This diagram indicates the design space of the counterweight. The mass of a counterweight can be determined by its location relative to the pitch axis and the target moment to counter. If the root pitching moment in hover at $C_T/\sigma = 0.12$ is chosen to be the target moment to nullify, Fig. 21 shows the resulting mass as a percentage of the blade mass. For example, if the counterweight is placed at a horizontal distance (dy) of 0.05 m and a vertical distance (dz) of 0.01 m from the pitch axis, it is 22 and 13% of the blade mass, respectively, for the quarter chord and midchord pitch axis design. A detailed design should take the support mass and control servo mass into account, but the midchord pitch axis design is expected to be significantly lighter.

C. Sectional Airloads

The sectional normal force is shown in Fig. 22. Comparing the rigid and flexible blades, the main difference occurs at the midspan

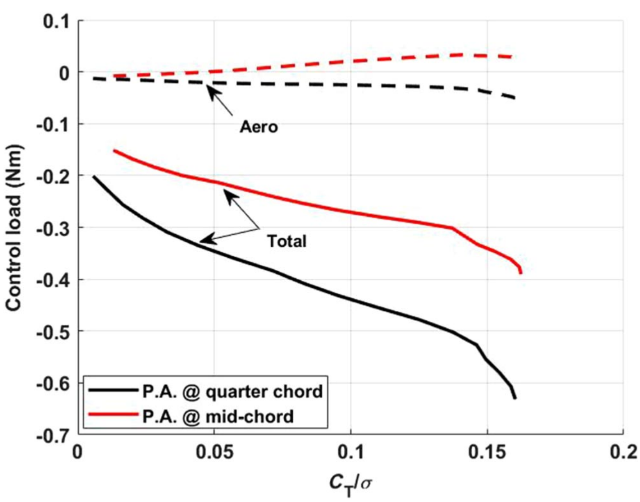

Fig. 19 Variation of blade control load with blade loading.

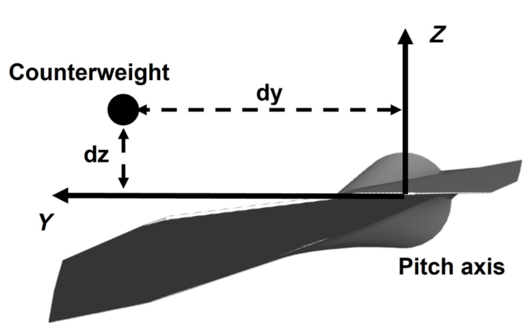

Fig. 20 Relative location of counterweight to pitch axis.

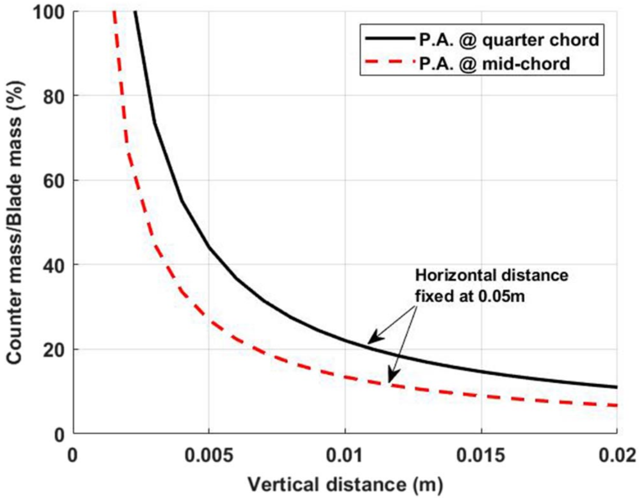

Fig. 21 Variation of counter mass with location (hover at $C_T/\sigma = 0.12$).

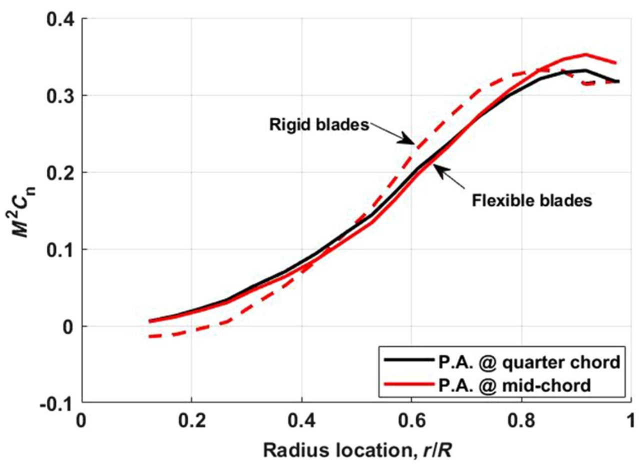

Fig. 22 Sectional normal force in hover ($C_T/\sigma = 0.12$).

range. The elastic twist explained in the blade deformation section alters the spanwise airload distribution. The midchord design has higher normal force at the tip portion. The chord force distribution is also affected by blade elastic deformation, but the magnitude is two orders lower than normal force (Fig. 23). At this thrust level, a large portion inboard of the blade has chord force toward the leading edge. The sectional pitching moment (Fig. 24) shows little difference with

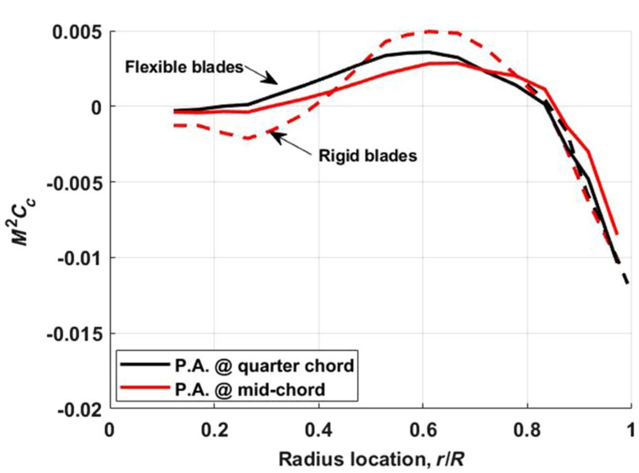

Fig. 23 Sectional chord force in hover ($C_T/\sigma = 0.12$).

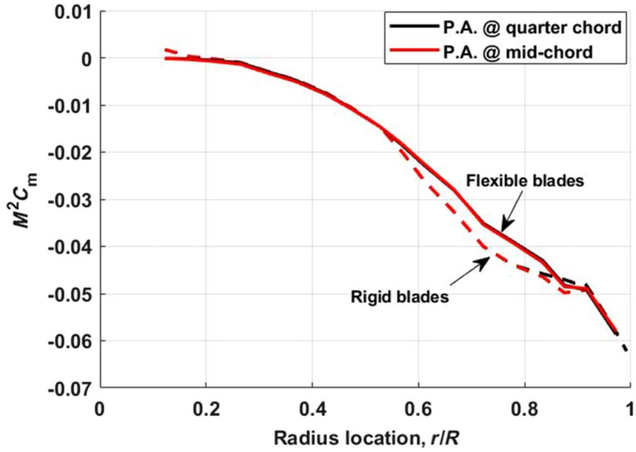

Fig. 24 Sectional pitching moment in hover ($C_T/\sigma = 0.12$).

or without flexibility. Both blade designs have the same nose-down aerodynamic pitching moment across the span.

D. Blade Response

A large C.G. offset combined with low torsional frequency raises the concern of blade stability, especially at high blade loading. The blade tip transient response to a perturbation is analyzed to check for potential stability problems (Fig. 25). By subtracting the algorithm damping ratio (2%), the flap damping ratio extracted from the response is about 2.5%. This value matches well with the elementary damping prediction ($\zeta = \gamma/16\nu_\beta \times 100$) of 2.2% based on the Lock number ($\gamma = 0.423$) and flap frequency ($\nu_\beta = 1.2$). This damping ratio is very small compared with the corresponding value on Earth's atmosphere ($\zeta_M/\zeta_E = 0.05$). The torsional damping ratio is also extracted and subtracted the algorithm damping ratio, which results in less than 1%. The persistent and prolonged oscillations are an artifact of the ultralow Lock numbers (which translate to low aerodynamic damping). This is a problem on Mars and merits separate and dedicated attention beyond the scope of this paper. The conclusions here are that moving the pitch axis location does not destabilize the blade any further than Lock number already does. It is perhaps likely that structural damping would be the dominate mechanism on Mars.

E. Three-Dimensional Stress

Three-dimensional FEA allows the direct examination of 3D stresses. All six stress components are available; the axial stress (σ_{xx}) and the in-plane shear stress (γ_{xy}) are examined in this section. The stresses reported here are in global coordinates: the X axis is the pitch axis positive toward the tip, the Y axis is in-plane and positive toward the leading edge, and the Z axis is aligned with the rotor shaft.

Figure 26 shows the axial stresses on the blade surface. The color map is tuned to highlight the stress pattern of the outboard portion. Compared with the midchord design, the baseline design has a stronger stress concentration at the midspan near the leading edge. This is mainly caused by the large lag force generated by the C.G. offset and the sudden decrease in stiffness caused by the spar end. For the midchord design, secondary high stress regions can be seen in the same spanwise location at the leading and trailing edges equally. This indicates that the sharp edges of the airfoil alone can raise the stress.

More interesting is the internal stress in the root region. Figure 27 compares the internal axial stress. It can be observed that there are stronger 3D patterns than the tip region. Stress concentration can be seen in the spar of both designs. Although it is possible to eliminate these concentrations by enlarging the transition portion, the current design goal is to preserve the aerodynamic design optimized by NASA while ensuring structural integrity with internal structural design. Therefore, a root cut out of 9%R was kept, leaving a small margin for the transition portion. Overall, the stress in both blade designs is well below the allowable strength of typical weave cloth

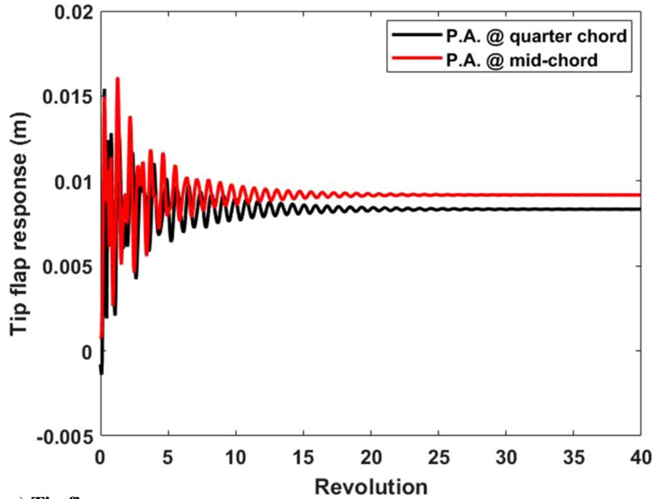

a) Tip flap response

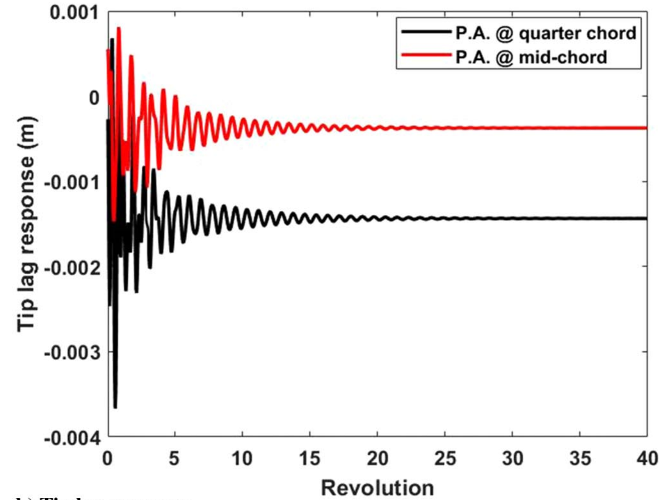

b) Tip lag response

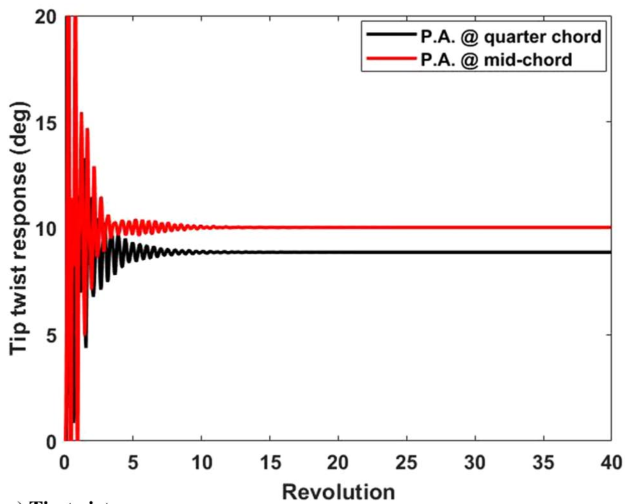

c) Tip twist response

Fig. 25 Blade tip response in hover ($C_T/\sigma = 0.12$).

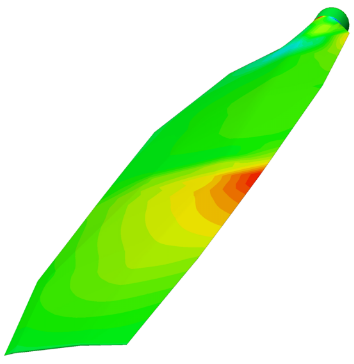

a) Quarter chord pitch axis design

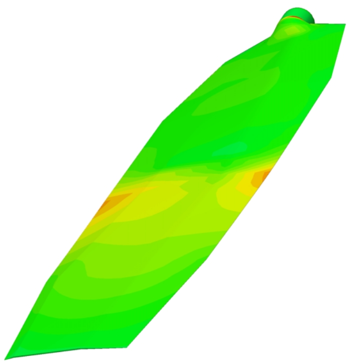

b) Mid-chord pitch axis design

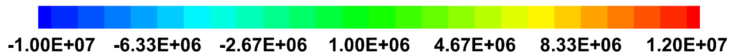

Fig. 26 Axial stress σ_{xx} in hover ($C_T/\sigma = 0.12$).

and unidirectional tape in low temperature: 750 and 900 MPa, respectively. For the quarter chord pitch axis design, the bottom and the leading edge of the spar are experiencing extension, whereas the top and trailing edge are in compression. This is due to the lift and the lag component of the centrifugal force from the large C.G. offset. In contrast, the midchord pitch axis design stress distributes more evenly, and the maximum stress is lower. Figure 28 shows the internal in-plane shear stress. Most of the shear stress is carried by the skin. The pattern of in-plane shear stress between the two blade designs is similar, but the magnitudes are different. This is caused by the smaller pitching moment acting on the midchord design blade.

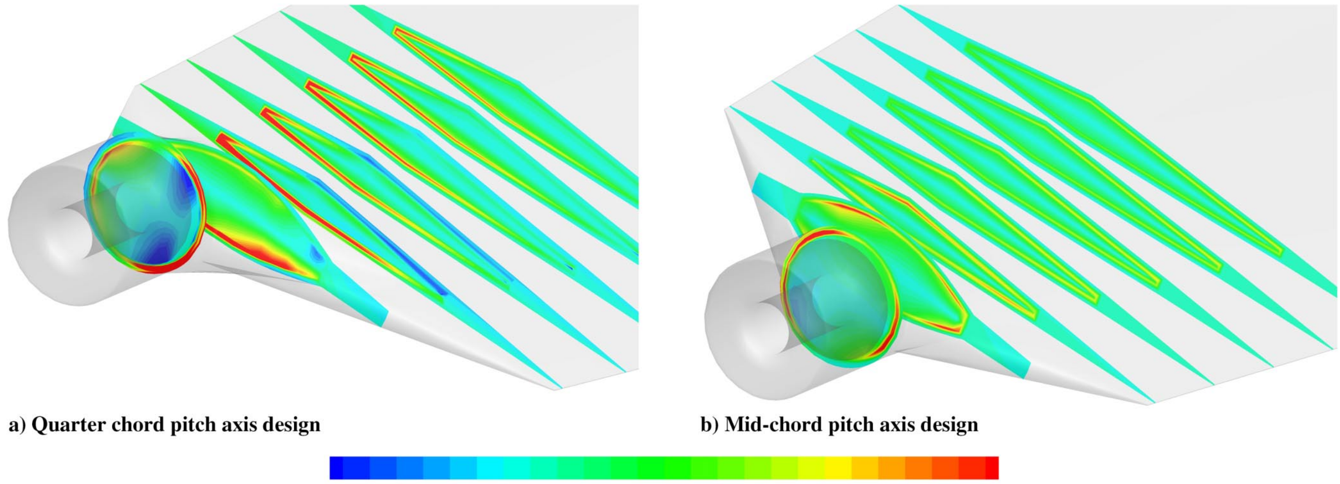

a) Quarter chord pitch axis design

b) Mid-chord pitch axis design

Fig. 27 Internal axial stress σ_{xx} in hover ($C_T/\sigma = 0.12$).

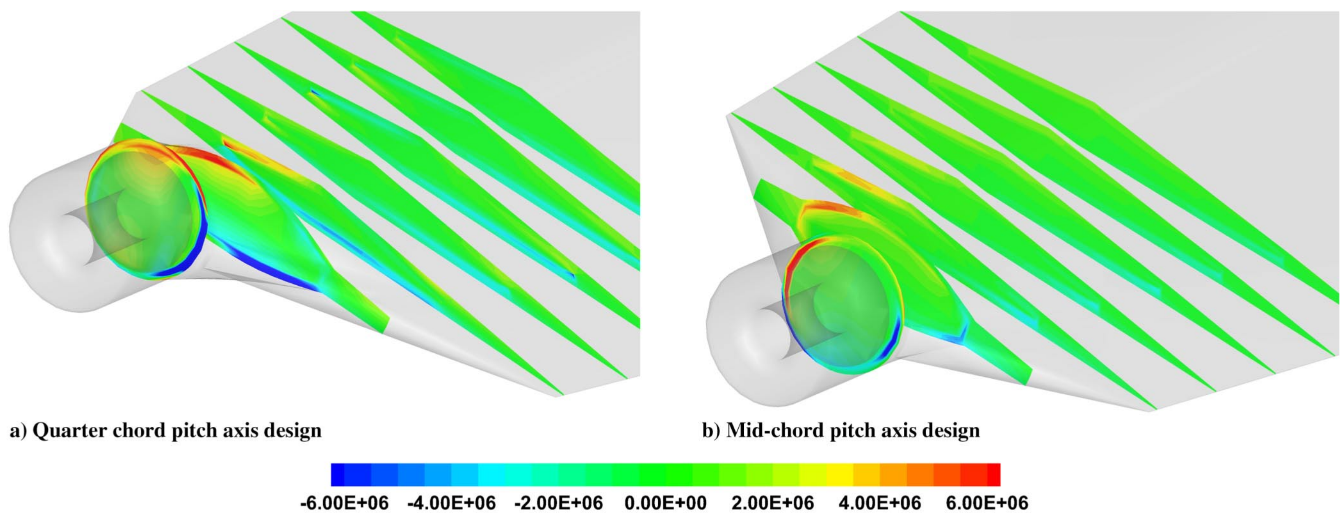

a) Quarter chord pitch axis design

b) Mid-chord pitch axis design

Fig. 28 Internal shear stress γ_{xy} in hover ($C_T/\sigma = 0.12$).

VII. Forward Flight Analysis

Before a detailed aeroelastic analysis can be conducted in forward flight, the aircraft pitch attitude and rotor states are needed. To obtain this, a multirotor aircraft trim analysis is performed.

A. Aircraft Trim Analysis

A vertex-first orientation of the hexacopter is considered (Fig. 29). Six four-bladed rotors are distributed evenly around the airframe. Rotors 1, 3, and 5 rotate in the clockwise direction, while the other three rotors turn counterclockwise for counter torque. Each rotor is identical. The vehicle parameters are listed in Table 5. A full vehicle analysis with flexible blades for all rotors and free wake is possible in principle but left for the future. The first pass is a simplified vehicle analysis to obtain control input for a detailed rotor analysis. A rigid blade flapping model is used with properties obtained from the 3D model (Table 6). A velocity sweep from hover to a cruise speed of 30 m/s was performed. The advancing blade tip Mach number reaches 0.93 at the highest speed. Figures 30 and 31 show the resulting required power and pitch and roll attitudes. The required power decreases as forward flight velocity increases, while the vehicle pitches forward to overcome the drag, and no roll motion is observed.

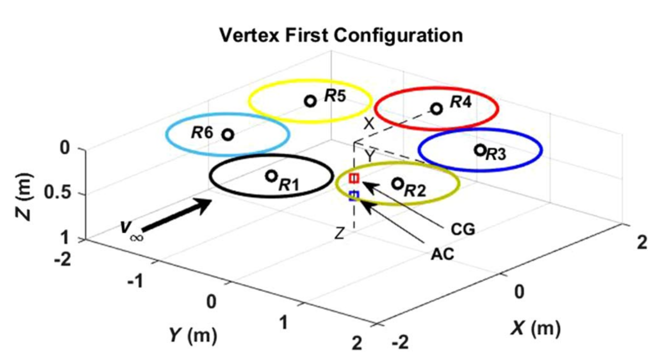

Fig. 29 Hexacopter trim model.

Table 5 Vehicle parameters

Parameter	Value
Gross takeoff weight (kg)	17.7
Center of gravity location (m)	[0, 0, 0.4]
Flat plate area (m^2)	0.49 5
Aerodynamic center location (m)	[0, 0, 0.6]
Hub location of rotor 1 (m)	[−1.344, 0, 0]

Table 6 Blade flapping model properties

Parameter	Value
Rotating flap frequency, ν_β (/rev)	1.2
Nonrotating flap frequency, $\omega_{\beta 0}$ (Hz)	11.9
Equivalent flap hinge offset, e (m)	0.099
Flap hinge stiffness, K_β ($\mathrm{N \cdot m/rad}$)	9
First moment of inertia of flapping, S_β ($\mathrm{kg \cdot m}$)	0.0059
Second moment of inertia of flapping, I_β ($\mathrm{kg \cdot m^2}$)	0.0016
Lock number, γ	0.423

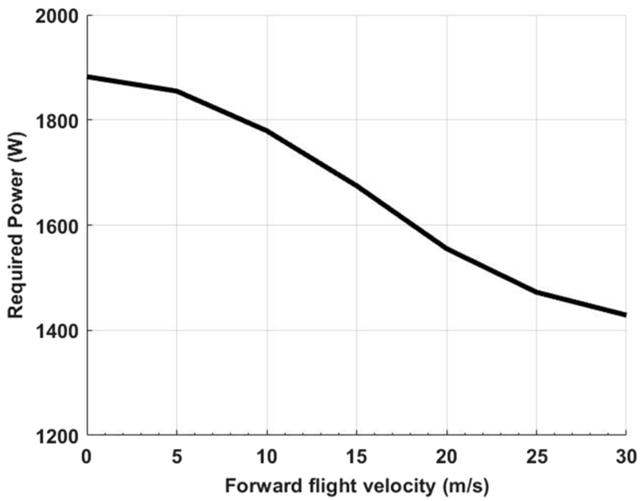

Fig. 30 Aircraft required power.

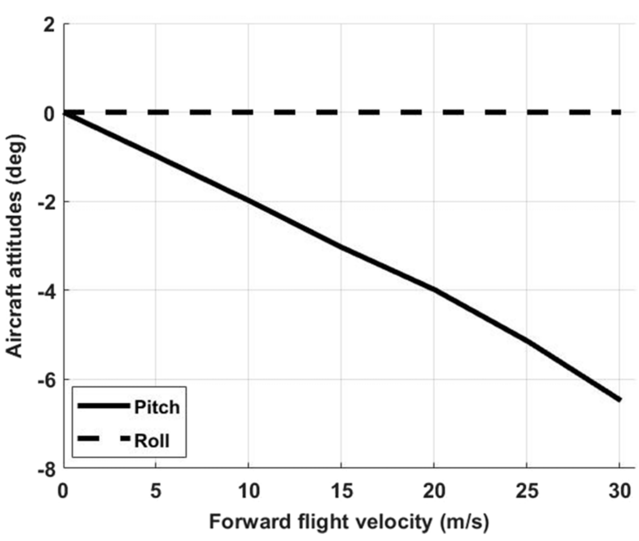

Fig. 31 Aircraft attitudes.

The collective pitch and blade loading of each rotor are shown in Figs. 32 and 33 (color code is the same as Fig. 29). Rotors 2 and 6 and rotors 3 and 5 share the same value due to symmetry. At the maximum cruise speed, rotor 4 has the largest collective and blade loading. This implies that the nose-down pitching moment generated by the airframe aerodynamic drag is not able to balance the nose-up hub pitching moment produced by the six rotors. Therefore, an extra nose-down pitching moment must be generated by the rotor thrusts.

With pitch attitude and max blade loading known, an isolated analysis is carried out by X3D with Maryland free wake (Table 7).

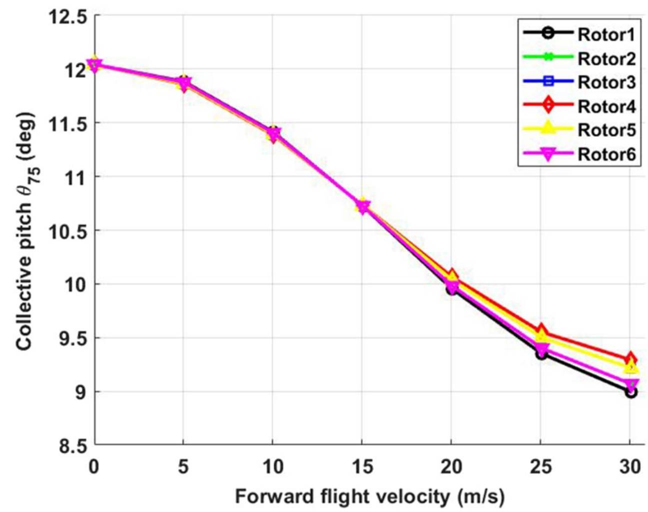

Fig. 32 Collective pitch at 75%R.

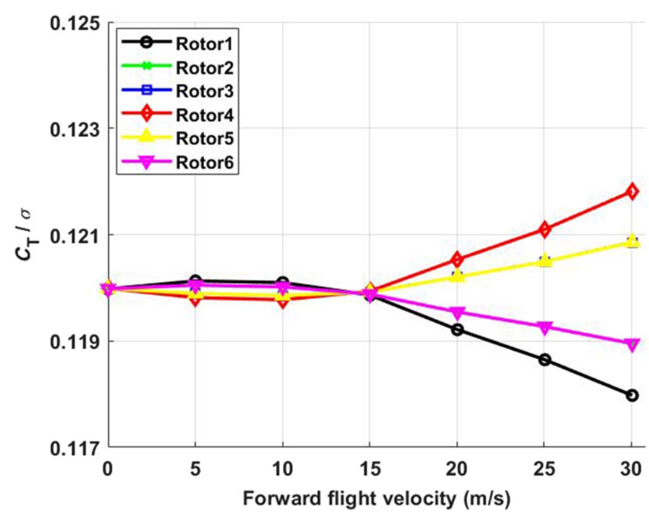

Fig. 33 Blade loading.

Table 7 Operating conditions of the forward flight analysis in X3D

Operating condition	Value
Blade loading	0.122
Shaft tilt	6.48°
Advance ratio	0.161
Collective control	10°
Max tip Mach	0.93
Max tip Reynolds	14,912

The rotor is trimmed to a blade loading of 0.122, the maximum on any of the rotors, at a forward shaft tilt angle of 6.48 deg, and an advance ratio of 0.161 (forward flight velocity of 30 m/s). The trimmed rotor operates under a collective of 10 deg. The assumption of an isolated rotor is not ideal because the rotor-to-rotor interaction will be left out in the analysis. However, the assumption is made for purposes of efficiency.

B. Sectional Airloads

Figure 34 shows the variation of sectional angle of attack (α) with Mach number at two locations: 30%R and 70%R. The highest angle of attack occurs near 180° azimuth, while the lowest happens in the

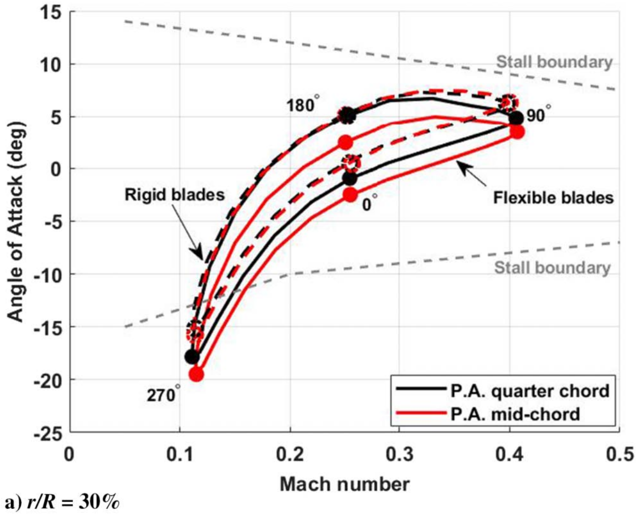

a) $r/R = 30\%$

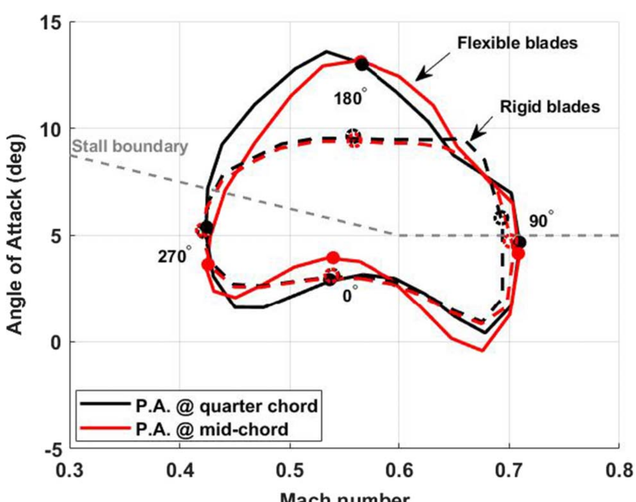

b) $r/R = 70\%$

Fig. 34 Angle of attack vs Mach number ($\alpha_s = -6.48°$, $\mu = 0.161$, $\theta_{75} = 10°$).

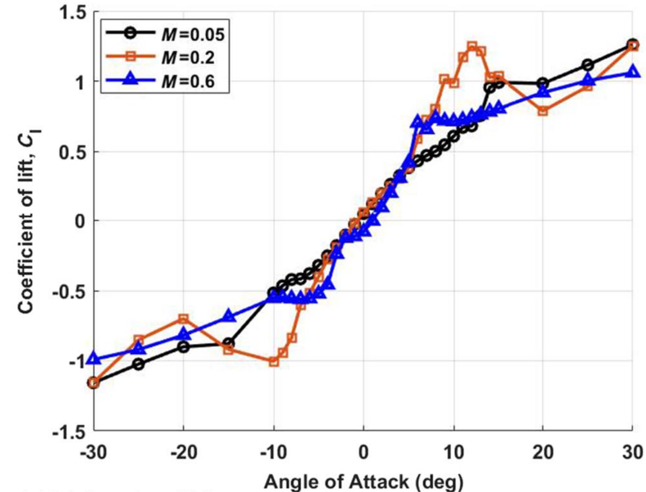

a) Airfoil at $r/R = 30\%$

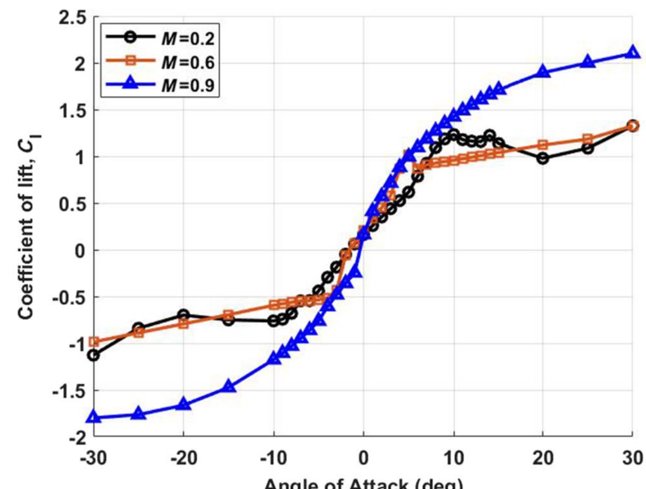

b) Airfoil at $r/R = 70\%$

Fig. 35 Coefficient of lift vs angle of attack [14].

first or fourth quarter of the rotor disk depending on the radial location. The outboard angle of attack of the advancing side and the retreating side is very similar. The features are quite different from the envelopes on a conventional rotor due to the high blade tip Mach number and the absence of cyclic control. The inboard region in the retreating side and the outboard region of the front disk operate beyond stall. Note that the stall boundary marked in Fig. 34 is the highest (and lowest) angle of attack of the linear portion of the lift coefficient curve (Fig. 35). For these unique airfoils, the stall angle of attack at high Mach are not as clear as conventional airfoils. Hence this does not necessarily mean that there is need for improvement to the current aerodynamic design. A higher-order aerodynamics model such as 3D RANS is eventually needed to understand the impact of this envelope. The objective here was to identify the critical area where such analysis would be needed.

Figures 36 and 37 compare the oscillatory sectional airloads. Most of the normal force is generated in the second quarter of the disk, which can be explained by the angle-of-attack distribution and the asymmetric flow condition of the advancing and retreating side. The inboard normal force at the advancing side of the disk is impacted the most by the blade deformation; however, the magnitude is still small. Further outboard, this impact shifts to the front of the disk. This is due to the change in angle of attack, which can be seen in Fig. 34b. Depending on the radial location, the front disk angle of attack predicted by the flexible blade model is 3–5° higher than the rigid blade model. On the other hand, the relocation of pitch axis has more influence on the rear disk area. The reason behind this difference can be traced back to angle of attack. For the pitching moments, the majority of the rotor disk produces a nose-down aerodynamic moment, except for the region close to the root. The pitching moments are very similar for two blade designs and are dominated by the 1/rev component.

C. Wake Geometry

The impulsive airloads in the first and fourth quarters of the rotor disk are from the wake, shown in Fig. 38. There is no significant difference in the wake of the two blade designs as expected. Overall, the trailers travel downstream quickly after the first rotor revolution. It can be seen that the trailers released from blades 3 and 4 interact with the advancing side and pass through the top side of the rotor. The trailers from blades 1 and 2 do not have any interactions with the blades. The low Re on Mars grows the core quickly, so the interactions might be less critical. Here, the core growth has not been relaxed by $1/Re$ for a conservative estimate of the loadings.

D. Control Load

The oscillatory control load of both blade designs are presented in Fig. 39. The control load is dominated here by a 2/rev variation because the torsion frequencies are close to 2/rev. The magnitude is similar to hover (Fig. 19), meaning that a majority of the control load still comes from the propeller moment. The control load with countermass is also shown. The addition of the countermass causes the pitch link to be relieved of constant compression.

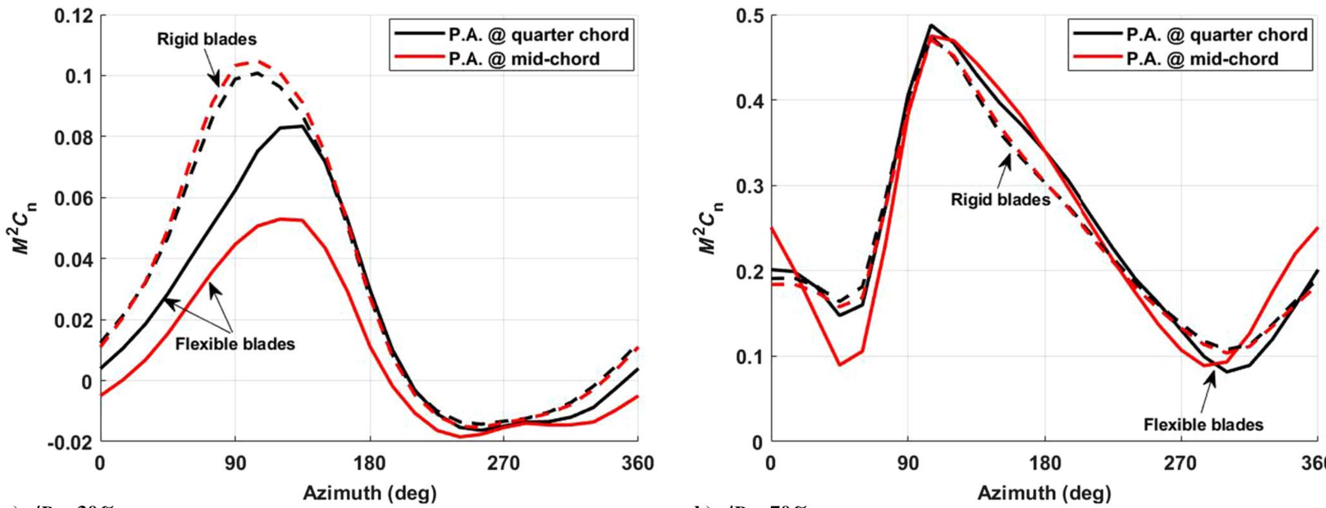

a) $r/R = 30\%$ b) $r/R = 70\%$

Fig. 36 Forward flight sectional normal force ($\alpha_s = -6.48°, \mu = 0.161, \theta_{75} = 10°$).

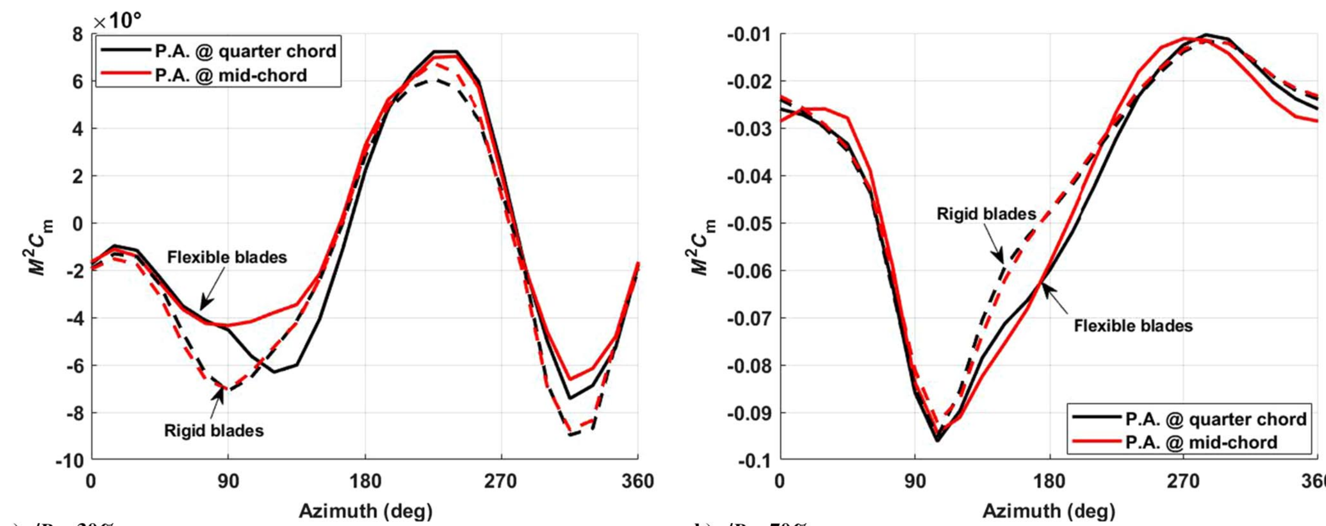

a) $r/R = 30\%$ b) $r/R = 70\%$

Fig. 37 Forward flight sectional pitching moment ($\alpha_s = -6.48°, \mu = 0.161, \theta_{75} = 10°$).

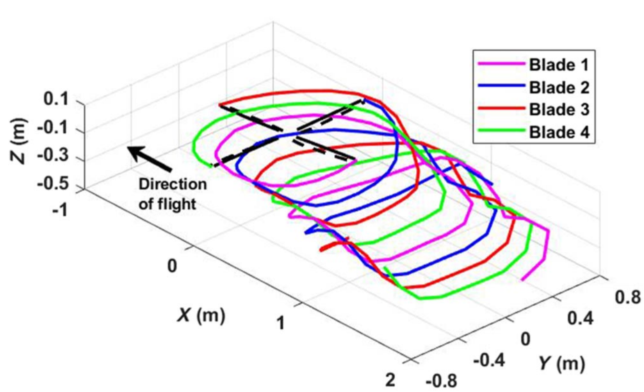

Fig. 38 Forward flight wake geometry of the baseline design ($\alpha_s = -6.48°, \mu = 0.161, \theta_{75} = 10°$).

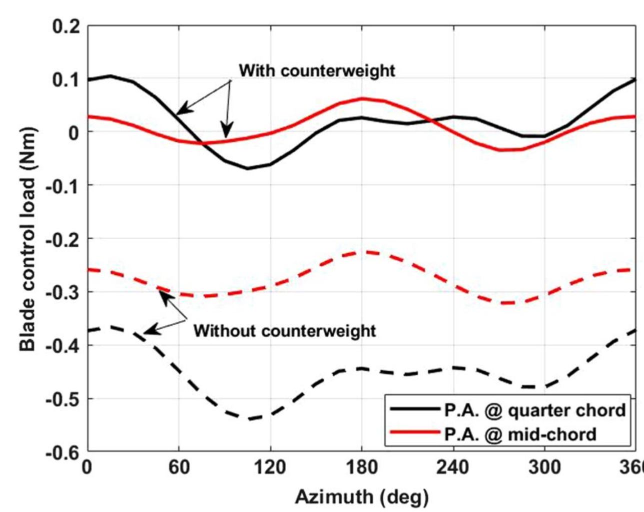

Fig. 39 Blade control load in forward flight ($\alpha_s = -6.48°, \mu = 0.161, \theta_{75} = 10°$).

E. Three-Dimensional Stress

The stress distribution varies with azimuth in forward flight. However, the patterns are very similar to that of in hover because of the dominance of centrifugal loading. Hence, the detailed stresses prediction at various azimuths are documented in Ref. [14] but not repeat here. The conclusions drawn from hover analysis retain in forward flight, except that a stress dip appears in the second quarter of the rotor disk for the quarter chord design but is not seen in the midchord design (Fig. 40). This result further proves that the midchord design is better regarding aeromechanical loading.

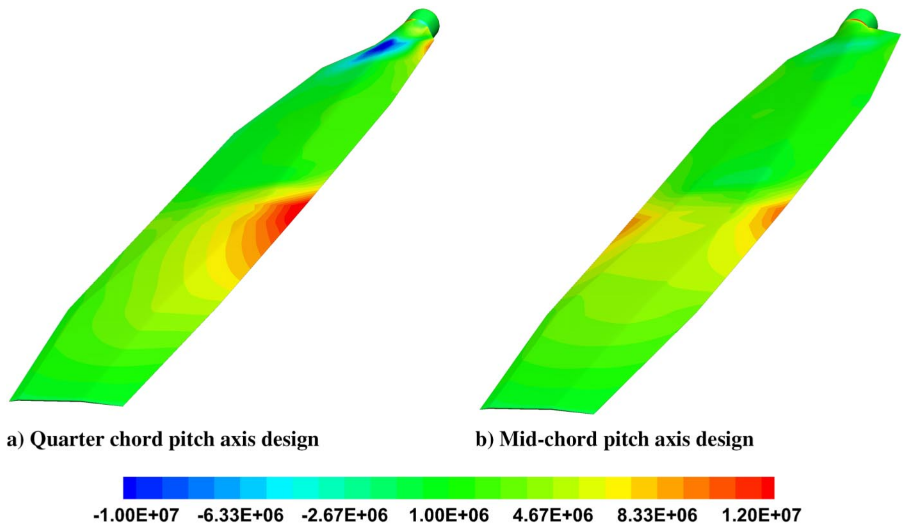

a) Quarter chord pitch axis design **b) Mid-chord pitch axis design**

Fig. 40 Blade axial stress σ_{xx} in forward flight ($\psi = 90°$, $\alpha_s = -6.48°$, $\mu = 0.161$, $\theta_{75} = 10°$).

VIII. Conclusions

An aeromechanical analysis of a conceptual future Mars hexacopter rotor was carried out in this paper. The objectives were to understand the interactions of rotor blade structural, aerodynamics, and controls on Mars and to prepare the tool chain needed for reliable design of such aircraft. Structural analysis in vacuum and comprehensive analysis in hover and forward flight were performed. Natural frequencies, blade response, control load, airloads, wake, and 3D stresses were studied for a baseline blade design with pitch axis at quarter chord and a midchord pitch axis design. During the course of this investigation, several key insights were obtained pertaining to an unusual Mars environment. Based on this, the following key conclusions are drawn:

1) The blade designs are feasible regarding aspects of natural frequency, stability, and 3D stresses.

2) A nose-up elastic twist deformation is observed in pure rotation, which is uncommon in conventional rotor blades. This phenomenon is due to the trapeze effect, which is amplified by the outboard portion of the blade having a 1% thickness-to-chord ratio and high structural twist. These features allow the trapeze effect to dominate over propeller moment, causing nose-up elastic pitch.

3) It may be beneficial to push the pitch axis back to midchord on Mars. By having the chordwise C.G. located closer to the pitch axis (without the help of leading-edge weight), the propeller moment is reduced by 30–40%, leading to a significantly lower control load. Moreover, the reduction of C.G. offset also removes the lag force generated by the in-plane component of the centrifugal force.

4) The countermass to balance the blade propeller moment in hover is 22% of blade mass for the quarter chord pitch axis design and 13% of blade mass for the midchord pitch axis design.

5) The blade flap, lag, and twist response to a perturbation indicate no instability for the blade designs. However, the ultralow Lock number leads to a low flap damping ratio of 2.5%, which implies persistent buzzing and fatigue loads for prolonged flight.

6) All blade designs have maximum stresses well below the material limits. Axial stress on the midchord pitch axis design is more evenly distributed, and there is a lower level of shear stress as well.

References

[1] Savu, G., and Trifu, O., "Photovoltaic Rotorcraft for Mars Missions," *31st AIAA/ASME/SAE/ASEE Joint Propulsion Conference and Exhibit*, AIAA/ASME/SAE/ASEE, San Diego, CA, July 1995, p. 2644.

[2] Young, L., "Vertical Lift—Not Just for Terrestrial Flight," *AHS/AIAA/RaeS/SAE International Powered Lift Conference*, Nov. 2000.

[3] Young, L., Aiken, E., Derby, M., Demblewski, R., and Navarrete, J., "Design Opportunities and Challenges in the Development of Vertical Lift Planetary Aerial Vehicles," *American Helicopter Society International Vertical Lift Aircraft Design Specialist's Meeting*, Jan. 2000.

[4] Young, L., and Edwin, W. A., "Vertical Lift Planetary Aerial Vehicles: Three Planetary Bodies and Four Conceptual Design Cases," *27th European Rotorcraft Forum*, Sept. 2001, pp. 45.1–45.18.

[5] Young, L., Gulick, V., and Briggs, G., "Rotorcraft as Mars Scouts," *Aerospace Conference*, Vol. 1, Inst. of Electrical and Electronics, Big Sky, MT, March 2002, pp. 1–378.

[6] Young, L., Aiken, E., Derby, M., Demblewski, R., and Navarrete, J., "Experimental Investigation and Demonstration of Rotary-Wing Technologies for Flight in the Atmosphere of Mars," *American Helicopter Society 58th Annual Forum*, American Helicopter Soc. Paper 64, June 2002.

[7] Datta, A., Roget, B., Griffiths, D., Pugliese, G., Sitaraman, J., Bao, J., Liu, L., and Gamard, O., "Design of a Martian Autonomous Rotary-Wing Vehicle," *Journal of Aircraft*, Vol. 40, No. 3, May 2003, pp. 461–472. https://doi.org/10.2514/2.3141

[8] Balaram, J., Daubar, I. J., Bapst, J., and Tzanetos, T., "Helicopters on Mars: Compelling Science of Extreme Terrains Enabled by an Aerial Platform," *9th International Conference on Mars*, California Inst. of Technology Paper 2089, July 2019.

[9] Pipenberg, T. B., Keennon, T. W., Langberg, A. S., and Tyler, D. J., "Development of the Mars Helicopter Rotor System," *75th American Helicopter Society Annual Forum*, Vertical Flight Soc. Paper 382, May 2019.

[10] Johnson, W., Withrow, S., Young, L., Malpica, C., Koning, W. J. F., Kuang, W., Fehler, M., Tuano, A., Chan, A., Datta, A., Chi, C., Lumba, R., Escobar, D., Bob Balaram, J., Tzanetos, T., and Grip, H. F., "Mars Science Helicopter Conceptual Design," NASA TM–2020–220485, March 2020.

[11] Chi, C., Lumba, R., Jung, Y. S., and Datta, A., "Preliminary Structural Design and Aerodynamic Analysis of Mars Science Helicopter Rotors," *ASCEND*, AIAA Paper 2020-4025, Nov. 2020.

[12] Grip, H. F., Johnson, W., Malpica, C., Scharf, D. P., Mandic, M., Young, L., Allan, B., Mettler, B., San Martin, M., and Lam, J., "Modeling and Identification of Hover Flight Dynamics for NASA–Mars Helicopter," *Journal of Guidance, Control, and Dynamics*, Vol. 43, No. 2, Feb. 2020, pp. 179–194. https://doi.org/10.2514/1.G004228

[13] Koning, W. J. F., Romander, E. A., and Johnson, W., "Optimization of Low Reynolds Number Airfoils for Martian Rotor Applications Using an Evolutionary Algorithm," *SciTech*, AIAA Paper 2020-0084, Jan. 2020.

[14] Chi, C., Lumba, R., and Datta, A., "Structural Design and Aeromechanical Analysis of a Next-Generation Mars Hexacopter Rotor," *77th American Helicopter Society Annual Forum*, Vertical Flight Soc. Paper 33, May 2021.

[15] Escobar, D., Chopra, I., and Datta, A., "High-Fidelity Aeromechanical Analysis of Coaxial Mars Helicopter," *Journal of Aircraft*, Vol. 58, No. 3, May 2021, pp. 1–15. https://doi.org/10.2514/1.C035895

[16] Datta, A., "X3D–A 3D Solid Finite Element Multibody Dynamic Analysis for Rotorcraft," *American Helicopter Society Technical Meeting on Aeromechanics Design for Vertical Lift*, Vertical Flight Soc. Paper 1, Jan. 2016.

[17] Chi, C., Datta, A., Chopra, I., and Chen, R., "Three-Dimensional Strains on Twisted and Swept Composite Rotor Blades in Vacuum," *Journal of Aircraft*, Vol. 58, No. 1, Jan. 2021, pp. 1–16. https://doi.org/10.2514/1.C035746

[18] Jung, Y. S., and Baeder, J. D., "$\gamma - \overline{Re_{\theta t}}$–Spalart–Allamaras with Crossflow Transition Model Using Hamiltonian-Strand Approach," *Journal of Aircraft*, Vol. 56, No. 3, May 2019, pp. 1040–1055. https://doi.org/10.2514/1.C035149

[19] Munday, P., Taira, K., Suwa, T., Numata, D., and Asai, K., "Nonlinear Lift on a Triangular Airfoil in Low-Reynolds-Number Compressible Flow," *Journal of Aircraft*, Vol. 52, No. 3, May 2015, pp. 924–931. https://doi.org/10.2514/1.C032983

[20] Yamauchi, G., and Johnson, W., "Trends of Reynolds Number Effects on Two Dimensional Airfoil Characteristics for Helicopter Rotor Analyses," NASA TM-84363, April 1983.

[21] Winslow, J., Otsuka, H., Govindarajan, B., and Chopra, I., "Basic Understanding of Airfoil Characteristics at Low Reynolds Numbers (10^4–10^5)," *Journal of Aircraft*, Vol. 55, No. 3, May 2018, pp. 1050–1061. https://doi.org/10.2514/1.C034415

[22] Koning, W. J. F., Romander, E. A., and Johnson, W., "Low Reynolds Number Airfoil Evaluation for the Mars Helicopter Rotor," *74th American Helicopter Society Annual Forum*, Vertical Flight Soc. Paper 169, May 2018.